Full-scale measurements of aerodynamic induction in a rotor plane

Larsen, Gunner Chr.; Hansen, Kurt Schaldemose

Published in:
Journal of Physics: Conference Series (Online)

Link to article, DOI:
10.1088/1742-6596/555/1/012063

Publication date:
2014

Document Version
Publisher's PDF, also known as Version of record

Full-scale measurements of aerodynamic induction in a rotor plane

2014 J. Phys.: Conf. Ser. 555 012063

(http://iopscience.iop.org/1742-6596/555/1/012063)

Full-scale measurements of aerodynamic induction in a rotor plane

Gunner Chr. Larsen and Kurt S. Hansen

Department of Wind Energy, *Technical University of Denmark*,
Building VEA-118,P.O.Box 49, Frederiksborgvej 399, DK-4000 Roskilde, Denmark

E-mail: gula@dtu.dk

Abstract. Reliable modelling of aerodynamic induction is imperative for successful prediction of wind turbine loads and wind turbine dynamics when based on state-of- the-art aeroelastic tools. Full-scale LiDAR based wind speed measurements, with high temporal and spatial resolution, have been conducted in the rotor plane of an operating 2MW/80m wind turbine to perform detailed analysis the aerodynamic induction. The experimental setup, analyses of the spatial structure of the aerodynamic induction and subsequent comparisons with numerical predictions, using the HAWC2 aerolastic code, are presented.

1. Introduction

One of the most essential tools in development of wind energy is reliable aero-elastic simulation packages, which enable detailed description of production, loading, control and dynamic stability of wind turbines conditioned on the inflow conditions. Basic elements in an aero-elastic package are an *aerodynamic model*, a model of the *control algorithm* and a *structural dynamic model* of the wind turbine structure.

The aerodynamic model is the link between the inflow wind field and the forcing of the wind turbine structural dynamic model. The Blade Element Momentum (BEM) method has turned out to be a fast, reliable and robust algorithm which, in combination with tabulated airfoil data, is by far the dominant aerodynamic approach used in state-of-the-art aero-elastic packages, although a number of basic assumptions are violated for the inflow conditions experienced in the atmospheric boundary layer (ABL).

The *aerodynamic induction*, describing the feed-back of the presence of the wind turbine (rotor) on the flow field, constitutes an important element in the BEM method, which directly links the tabulated airfoil data to the forcing of the rotor. This paper presents results from the first ever full-scale recordings of aerodynamic induction in the rotor plane of an operating rotor and compares these with analogous simulated inductions using the aeroelastic package HAWC2 [1].

An alternative approach to the present full-scale measurements could be to base an experimental analysis of wind turbine rotor induction on wind tunnel measurements using e.g. PIV. However, to obtain realistic inflow conditions, emulating the turbulent characteristics of the atmospheric boundary layer, is a challenge in itself, and on top of that comes aerodynamic challenges associated with low Reynolds number wind tunnel flows as well as production and characterization of model blade profiles (i.e. lift, drag and moment coefficients) with sufficient accuracy for use in aeroelastic simulations.

Finally, carrying out PIV recordings directly in rotor plane would also require some refinements of this measuring technique. In conclusion, we therefore believe that full-scale measurements of the aerodynamic induction in the rotor plane of an operating turbine provide valuable input to detailed validation of the aerodynamic module of aeroelastic codes, which is not straightforwardly obtained from wind tunnel studies.

2. Experimental Setup

The experimental campaign was conducted in the Tjæreborg wind farm, which is located in the western part of Denmark. This wind farm consists of 8 × 2.5 MW wind turbines, each with a diameter of 80m. One of the turbines was equipped with a spinner mounted up-wind looking LiDAR system scanning along a vertical oriented circular pattern, with the plane of this circular pattern being (approximately) perpendicular to the mean flow direction. This LiDAR system provides a reference for the undisturbed inflow conditions. Supplementing reference wind speed recordings are available from a 93m high reference meteorological mast located approximately four rotor diameters from the instrumented turbine.

For selected mean wind directions, where the inflow of the instrumented turbine was unaffected by the wakes of the other turbines, a 2D LiDAR system [2], [3], which is able to resolve one wind field velocity component in a plane, was mounted on a movable crane lift placed downstream in a direction perpendicular to the rotor plane of the investigated turbine, thus enabling successive scanning campaigns of different parts of the rotor plane. The applied LiDAR system is of the focused continuous-wave (CW) type offering high temporal and spatial resolution. However, the LiDAR beam averaging volume depends significantly on the focus distance. Therefore, and because the LiDAR laser beam has a moderate opening angle, resolving flow characteristics in the rotor plane cross section involves a compromise on the focus distance, where a large focus distance enables a large scanning area but on the cost of a large averaging volume, which in turn potentially compromises the resolution of the rotor plane flow characteristics. For the conducted tree campaigns a focus distance (FC) of 56m was chosen, thus resulting in tree disjunctive rotor plane scanning areas as shown in Figure 1.

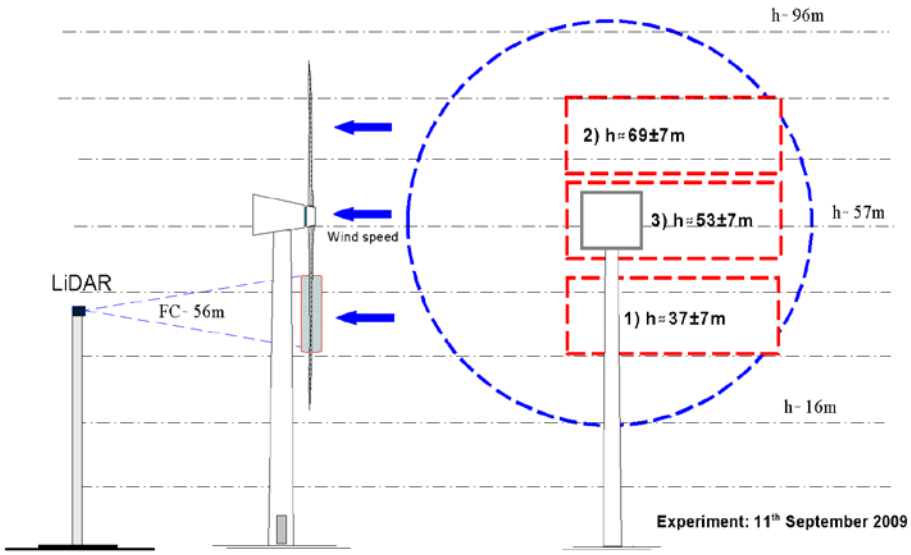

Figure 1: Experimental setup for rotor plane speed measurements.

Figure 1 illustrates the experimental setup established for measuring horizontal wind vector components in the rotor plane of the operating NM80m wind turbine. The 2D LiDAR system was positioned at 3 different heights above ground level (i.e. 37m, 53m and 69m) corresponding to the scanning areas denoted by 1), 2) and 3), respectively. As seen, the scanning areas 1–3 allow for resolving the mean rotor induction as function of height and thus implicitly as function of wind speed due to the wind shear.

The measured full-scale dataset consists of 21 10-minute sequences covering the (undisturbed) mean wind speed regime between 7.6 m/s and 9.1m/s at hub height, and each consisting of upstream reference recordings of the ambient flow field as well as directly measured high resolution flow characteristics in the rotor plane.

3. Analysis Method

Rotor induction is traditionally decomposed in axial- and tangential induction describing rotor (pressure) feed-back on the along wind velocity and the vorticity, respectively. The present results relate primarily to the *axial induction*, as only one velocity component is resolved by the applied LiDAR systems.

The axial induction factor, a, is defined as

$$a(r,\theta) = 1 - \frac{U_{rp}(r,\theta)}{U_{\infty}(r,\theta)} \tag{1}$$

where $U_{rp}(r,\theta)$ denotes the along wind rotor plane wind speed at the rotor spatial point (r,θ), $U_{\infty}(r,\theta)$ is the undisturbed upstream mean wind speed, and (r,θ) are polar coordinates, with r denoting the radial coordinate and θ denoting the azimuthal coordinate. With the definition formulated in equation (1), we implicitly assume that the tangential induction can be neglected *upstream* the rotor plane, which is correct in a first order approximation [4]. Note that in the present analysis, the quantities in equation (1) are understood as *mean values*, which to some extend is consistent with the Blade Element Momentum (BEM) assumption of stationary flow conditions.

For the numerical analysis, the quantities entering equation (1) can be extracted directly from HAWC2 simulations. The analysis of the full scale LiDAR recordings is slightly more complicated for the following reasons: 1) Only the velocities along the LiDAR laser beam is recorded (i.e. the line of sight velocity), which in most recording cases differ from the mean flow direction; 2) Moving blades in the rotor plane trigger the LiDAR Doppler shift based recording system; 3) Possible wind veer and turbine yaw misalignment are not directly measured, but has to identified from the recordings resulting from the up-wind looking LiDAR; and 4) The orientation of the 2D LiDAR system scanning the rotor plane must be defined. The above complications are accounted for in the following sub-sections.

3.1. From Line of Sight Velocities to Axial Velocities

The LiDAR systems provide information on instantaneous wind speeds in the *line of sight* (los) of the laser beams only, and a transformation is therefore needed to compensate for the involved laser beam tilt, pan and yaw angles to arrive at flow field characteristics in the mean wind direction. A first order approximation is suggested in [5] which reads:

$$U(\boldsymbol{x}(t),t) = \overline{U}(\boldsymbol{x}(t)) + u(\boldsymbol{x}(t),t) = \frac{U_{los}(\boldsymbol{x}(t),t)}{\cos(\theta_p(t))\cos(\theta_t(t))} \tag{2}$$

where U is the longitudinal wind speed, $\boldsymbol{x}$ is a vector identifying a point in space, t is the time, u is the longitudinal turbulence component, an upper bar indicates mean value, and lower index “los” indicate LiDAR line-of-sight velocities. The time dependent angles θ_p and θ_t denote the LiDAR laser beam pan and tilt angles, respectively, where θ_p is given with reference to the wind turbine nacelle orientation, and θ_t usually is given with reference to a plane parallel with the (average) ground surface - even if we are dealing with a turbine with the nacelle tilted relative to the ground surface. The latter convention

makes sense, since the average flow field in focus has stream lines parallel to the ground surface for not too complex terrain conditions. For complex terrain conditions the LiDAR recording technique is in general challenged. In the present analysis we will assume that the terrain in question is flat and homogeneous. Note, that the transformation defined in equation (2) applies for both the involved LiDAR systems.

3.2. Impact of Moving Blades

The LiDAR technology basically utilizes the Doppler shift associated with (laser) light scatter of moving aerosols [2], but responds equally well on any other moving object such as the rotating rotor. Therefore dedicated filters are established to eliminate the LiDAR response of the moving blades associated with the rotor plane recordings. A moving blade results in a signal spike, while the fixed tower results in a zero wind speed recording, and therefore a simple filtering approach, discharging recorded wind speed values outside the wind speed range 0.1-20 m/s, was implemented.

3.3. Identification of Wind Veer and Yaw Misalignment

Even though perfect yaw alignment is aimed at, rotor yaw misalignment cannot be completely avoided in practice. This has derived consequences for the inflow conditions and thus the aerodynamic induction. It is therefore of interest to identify possible yaw errors during the recording campaigns. To achieve the best possible accuracy we suggests a new dedicated approach, which rely on the LiDAR based rotor inflow fields measurements only. This is advantageous, because these are temporally/spatially well correlated with the rotor inflow characteristics.

We consider LiDAR recordings performed from the nacelle of a wind turbine. In the ideal case of no wind turbine yaw error and no tilt of the LiDAR (i.e. no tilt of the nacelle or, alternatively, a LiDAR setup compensating for a possible tilt of the nacelle), the *longitudinal* wind speed measurement, at the spatial point $\boldsymbol{x}$ at time t, may be approximated from the line-of-sight LiDAR recording as described in equation (2).

In case the wind turbine operates with a yaw error, the line-of-sight LiDAR recording is pan-wise off with the wind turbine yaw error, θ_y, relative to the flow coordinate system aligned along the mean wind direction. In such cases, equation (2) is modified to

$$U(\boldsymbol{x}(t),t)=\overline{U}(\boldsymbol{x}(t))+u(\boldsymbol{x}(t),t)=\frac{U_{los}(\boldsymbol{x}(t),t)}{\cos(\theta_p(t)+\theta_y(t))\cos(\theta_t(t))} \tag{3}$$

In case the yaw error is not recorded, we can use the relationship in equation (3) to estimate the yaw error in periods with constant yaw error; i.e. no wind turbine yaw activity and constant wind direction. In this case, the yaw error is constant at a *given altitude*, and equation (3) simplifies to

$$U(\boldsymbol{x},t)=\overline{U}(\boldsymbol{x})+u(\boldsymbol{x},t)=\frac{U_{los}(\boldsymbol{x},t)}{\cos(\theta_p(t)+\theta_y(\theta_t(t)))\cos(\theta_t(t))} \tag{4}$$

The ensemble averaged version of relation (4) reads

$$\overline{U}(\boldsymbol{x})=\frac{\overline{U}_{los}(\boldsymbol{x})}{\cos(\theta_p+\theta_y(\theta_t))\cos(\theta_t)} \tag{5}$$

where the tilt and pan angles are dictated by the spatial point, $\boldsymbol{x}$, to which the recording relates.

We now consider pairs of pan angles of the form ($\theta_{p,i}$,-$\theta_{p,i}$), where i identifies the i'th pair of this type and defines

$$\begin{aligned}\overline{U}_{los,+}(\theta_t,i)&=\overline{U}(\theta_t)\cos(\theta_{p,i}+\theta_y(\theta_t))\cos(\theta_t)\\&=\overline{U}(\theta_t)\left[\cos(\theta_{p,i})\cos(\theta_y(\theta_t))-\sin(\theta_{p,i})\sin(\theta_y(\theta_t))\right]\cos(\theta_t)\end{aligned} \tag{6}$$

and

$$\begin{aligned}\overline{U}_{los,-}(\theta_t,i) &= \overline{U}(\theta_t)\cos\left(-\theta_{p,i}+\theta_y(\theta_t)\right)\cos(\theta_t)\\ &= \overline{U}(\theta_t)\left[\cos(\theta_{p,i})\cos(\theta_y(\theta_t))+\sin(\theta_{p,i})\sin(\theta_y(\theta_t))\right]\cos(\theta_t)\end{aligned} \tag{7}$$

in which we have utilized, that for a flat and homogeneous terrain the ensemble averaged mean wind speed depends on the height above terrain only (i.e. the tilt angle only).

From equations (6) and (7) we derive the following two relationships

$$\overline{U}_{los,-}(\theta_t,i)-\overline{U}_{los,+}(\theta_t,i) = 2\overline{U}(\theta_t)\sin(\theta_{p,i})\sin(\theta_y(\theta_t))\cos(\theta_t) \tag{8}$$

and

$$\overline{U}_{los,-}(\theta_t,i)+\overline{U}_{los,+}(\theta_t,i) = 2\overline{U}(\theta_t)\cos(\theta_{p,i})\cos(\theta_y(\theta_t))\cos(\theta_t) \tag{9}$$

Reformulating these equations as

$$\sin(\theta_y(\theta_t)) = \frac{\overline{U}_{los,-}(\theta_t,i)-\overline{U}_{los,+}(\theta_t,i)}{2\overline{U}(\theta_t)\sin(\theta_{p,i})\cos(\theta_t)} \tag{10}$$

and

$$\cos(\theta_y(\theta_t)) = \frac{\overline{U}_{los,-}(\theta_t,i)+\overline{U}_{los,+}(\theta_t,i)}{2\overline{U}(\theta_t)\cos(\theta_{p,i})\cos(\theta_t)} \tag{11}$$

we finally arrive at

$$\tan(\theta_y(\theta_t)) = \frac{\overline{U}_{los,-}(\theta_t,i)-\overline{U}_{los,+}(\theta_t,i)}{\overline{U}_{los,-}(\theta_t,i)+\overline{U}_{los,+}(\theta_t,i)}\cot(\theta_{p,i}) \tag{12}$$

or

$$\theta_y(\theta_t) = \mathrm{ArcTan}\left(\frac{\overline{U}_{los,-}(\theta_t,i)-\overline{U}_{los,+}(\theta_t,i)}{\overline{U}_{los,-}(\theta_t,i)+\overline{U}_{los,+}(\theta_t,i)}\cot(\theta_{p,i})\right) \tag{13}$$

We notice, that the estimated yaw error depends on the tilt angle (i.e. altitude) only, and consequently the best possible estimate of the yaw error is obtained by averaging the relation in equation (13) over all available pan angle pairs; viz.

$$\widetilde{\theta}_y(\theta_t) = \underset{i}{E}\left[\mathrm{ArcTan}\left(\frac{\overline{U}_{los,-}(\theta_t,i)-\overline{U}_{los,+}(\theta_t,i)}{\overline{U}_{los,-}(\theta_t,i)+\overline{U}_{los,+}(\theta_t,i)}\cot(\theta_{p,i})\right)\right] \tag{14}$$

in which E[$*$] denotes the mean value operator. We finally note, that relation (14) also may be used to quantify wind veer over a flat and homogeneous terrain regardless if the wind turbine is operating with a yaw error or not.

In case we are dealing with a "forward looking" LiDAR scanning in a conical pattern from a tilted orientation (i.e. aligned with a tilted nacelle), the tilt angle requested in equation (14) may be derived from the time dependent scanning azimuthal angle, $\theta_a(t)$, and the wind turbine rotor tilt angle, θ_{wt}, as

$$\theta_t = \theta_{wt} + \theta_c \sin\theta_a(t) \tag{15}$$

where θ_c is the LiDAR opening angle defining the conical scan pattern. Note, that zero azimuth angle in the above formulation corresponds to zero "additional" tilt from the conical scan pattern, and that the sign convention is such, that $\theta_a(0+) = 0+$ corresponds to a small positive "additional" tilt.

3.4. Orientation of rotor scanning LiDAR

For the present investigation, yaw misalignment is not only an issue for the nacelle LiDAR, but also for the 2D LiDAR scanning into the rotor plane. For the 2D LiDAR system, the yaw misalignment can in principle also be identified using the approach described above, if applied to a measuring sequence in which the turbine is in a stand still situation. However, only a reduced scanning regime can be applied, in which the tower shadow effects are excluded. This is to avoid tower induced flow asymmetries around zero pan angle. Finally, emphasis has to be put on relatively large pan angles because of the $\cot(\theta_{p,i})$ "weighting factor" in equation (14), which tends to amplify small uncertainties in the relevant associated differences in the line-of-sight velocities dramatically for small pan angles.

In this analysis, it was found more appropriate to base identification of the 2D LiDAR orientation, relative to the mean wind direction, on recorded *free flow* conditions from campaign 1 and 2, respectively. The requested, *altitude dependent*, 2D LiDAR yaw errors can be estimated directly from these using equation (5). The 2D LiDAR yaw orientation referring to campaign 3 was taken as an arithmetic mean of the yaw orientations referring to campaign 1 and 2, motivated by the mean altitude of campaign 3 recordings being the average of mean altitudes associated with campaign 1 and 2 recordings.

4. Numerical Approach

The inflow conditions, associated with the full-scale dataset, are derived from the upwind scanning LiDAR system using the approach described in the previous section. With inflow conditions matching the measurements defined, the axial induction at arbitrary points in the rotor plane can be modelled using the state-of-the-art aeroelastic code HAWC2.

The structural part of this code is based on a multi-body formulation as described in [6] using the floating frame of reference method. Each body includes its own coordinate system with calculation of internal inertia loads, when this coordinate system is moved in space, and hence large rotation and translation of the body motion are accounted for, thus providing a fully non-linear kinematic formulation.

The aerodynamic part of the code is based on the BEM theory, but extended from the classic approach to handle dynamic inflow, dynamic stall, skew inflow, shear effects on the aerodynamic induction and effects from large deflections to match the non-linear kinematic formulation of the structural part. The induced velocities are calculated based on the *local* inflow velocities, thus resulting in different induction of the upper and lower part of the rotor, respectively, in case of a inflow wind shear [7]. Turbine operational conditions (i.e. pitch setting and rotor speed) were obtained from the turbine SCADA system.

5. Results

The recorded data set defines the potential turbine operational conditions to be investigated. The full dataset consists of 21 10-minute periods, and a subset of three 10-minute sequences is investigated in this paper. The characteristics of those are specified in Table 1.

Table 1: Characteristics of LiDAR scanning and the wind turbine operation.

Record id.	Wind speed [m/s]	Turbulence intensity [%]	Rotational speed [rpm]	Pitch angle [deg.]	yaw misalign ment	Campaign no.
200909111400	8.7	15	16.2	-1.0	1°[1)]	1
200909111600	8.2	15	16.2	-4.5	-3°	2
200909111630	8.4	15	16.2	-1.0	-3°	3

[1)] Derived from turbine nacelle position recordings combined with mean wind direction recordings from the meteorological mast, as nacelle LiDAR recordings was not available for this measuring period.

In addition to the operational characteristics given in Table 1, the wind shear as well as the wind veer of the inflow field must be identified. This is conveniently done using the approach outlined in Section 3 combined with the spinner LiDAR recordings, which offer a high spatial resolution and the best possible correlation with the "true" rotor inflow characteristics. As an illustrative example, the results extracted from campaign 3 are shown in Figure 2, and from this analysis an estimated wind shear exponent of 0.12 is obtained and subsequently used in the numerical study. Also shown on Figure 2 is the shear as derived from the meteorological mast recordings. As seen these agree except for an offset, which is due to turbine induced wake effects at the mast position. The recorded wind veer is not resolved in detail in the present numerical study but approximated with an inflow yaw error (YM) defined as the mean wind veer over the rotor.

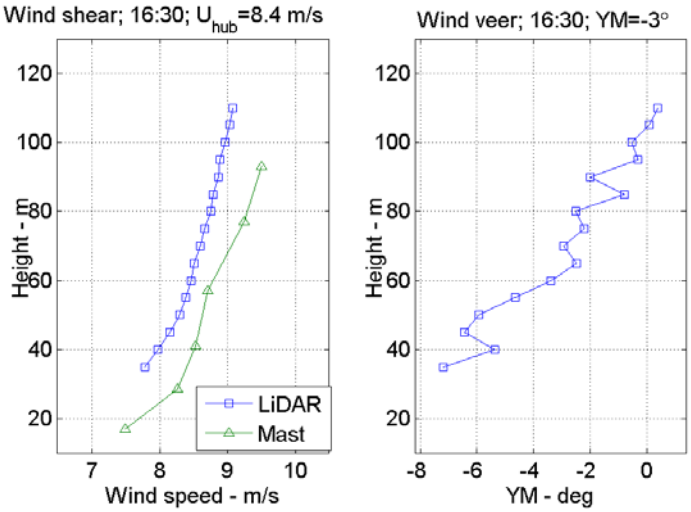

Figure 2: Wind shear and wind veer recorded with the spinner LiDAR as based on campaign 3.

The aerodynamic induction depends on the *inflow velocity*, the *pitch setting* of the blade and the *aerodynamic characteristics* of the rotor. As the latter varies with the radial distance, the axial induction is a priori expected to potentially depend on the radial coordinate as indicated in equation (1). The dependence on the inflow velocities is, in this investigation, reflected partly by the different 10-minute runs referring to different ambient mean wind speeds, and partly by the inherent inflow wind shear. The latter is reflected in equation (1) by the azimuth angle dependence. However, it should be noted, that the mean wind speed variations over the rotor, as well as among the available 10-minute runs, are small for the present data set.

To eliminate the effect from varying mean inflow conditions, the dependence of the axial induction with the rotor radial coordinate (i.e. the rotor *aerodynamic characteristics*) is investigated by considering the induction within "horizontal slices" of the scanning areas illustrated in Figure 1. For this purpose a lateral coordinate (y) is introduced with zero at the centre tower location. With this approach, the results from scanning area 3, representing blade(s) with an approximately horizontal orientation and thus with only marginal influence from wind shear, offers a direct resolution of the axial induction as function of the (physical) rotor radial coordinate, given the operational conditions associated with this campaign.

As for the scanning areas 1 and 2, the y-coordinate serves as a "stretched" radial coordinate, which relates to the physical radial coordinate, r, as

$$y = r\cos(\theta_a) \tag{16}$$

where the azimuthal coordinate, θ_a, is assumed to be zero for the blade being in a horizontal position. For these scanning areas, the non-linear coordinate transformation (16) thus emphasizes the behavior of the axial induction for the outer part of the rotor.

Figures 3-5 show the axial induction as function of the lateral coordinate normalized with the rotor radius (R), y/R, for a variety of altitudes referring to the invested campaigns. As the experimental values do not refer to a priori defined distinct points, the shown inductions refer to averages over $1\times1\text{m}^2$ segments in the cross section in question.

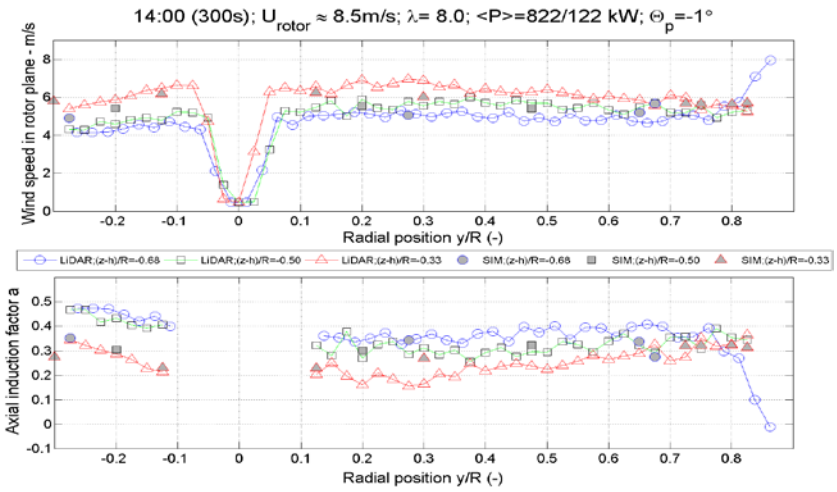

Figure 3: Axial induction as function of lateral coordinate (y/R) as based on campaign 1 data.

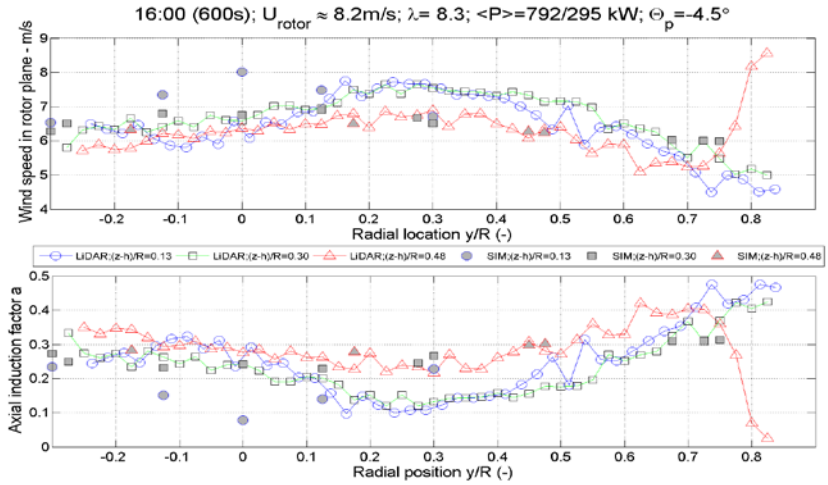

Figure 4: Axial induction as function of lateral coordinate (y/R) as based on campaign 2 data.

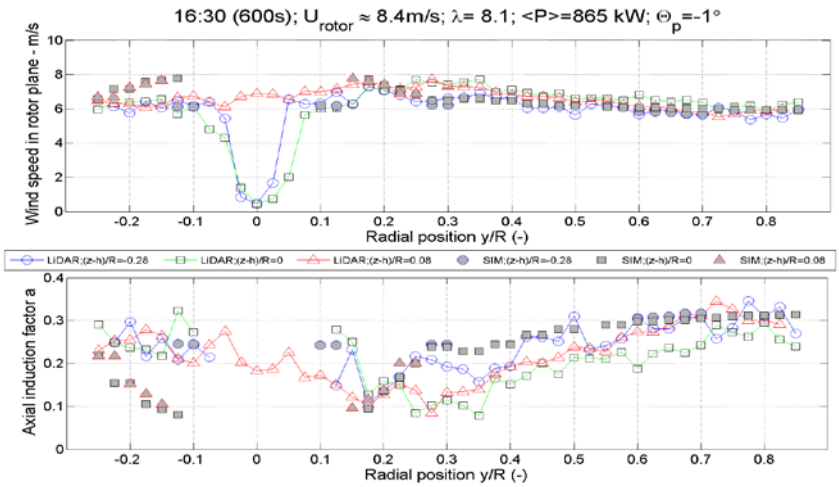

Figure 5: Axial induction as function of lateral coordinate (y/R) as based on campaign 3 data.

In an attempt to resolve the potential dependence of the axial induction on the *inflow wind speed*, a vertical coordinate, z, is introduced. The idea is to take advantage of the (moderate) wind shear, and Figure 6 shows the axial induction as function of a normalized vertical coordinate centered at hub height (h), $(z-h)/R$, conditioned on selected blade radii (i.e. selected blade aerodynamic characteristics).

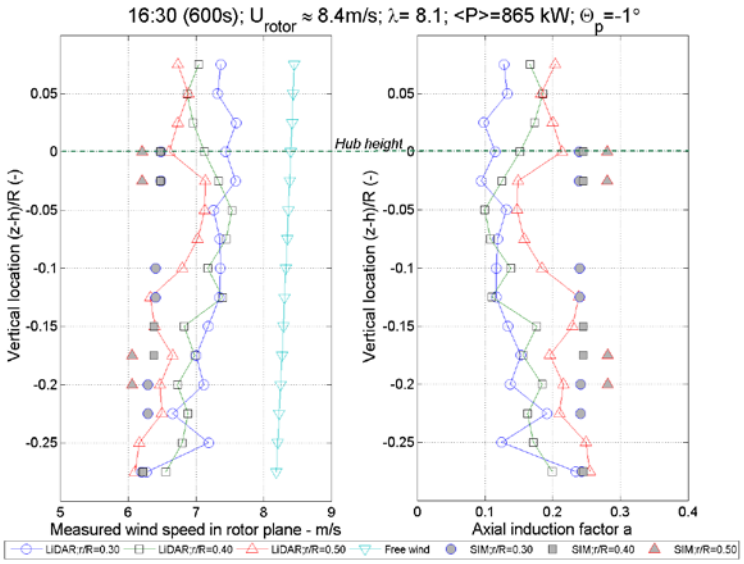

Figure 6: Axial induction as function of vertical coordinate $(z-h)/R$ as based on campaign 3 data.

6. Discussion

Concerning the dependence of the axial induction on the *aerodynamic characteristics* of the blade cross sections, Figure 5 shows measured and computed values in horizontal cross sections with altitudes at and close to the hub height of the turbine. The computational grid for the aerodynamics in the HAWC2 platform is of a polar type, and for the azimuthal configuration in question a large number of grid points are available, thus providing a good spatial resolution of the numerical predictions. It is observed, that there is a fair agreement between computed and measured values over the entire radial regime, and that the expected increase in aerodynamic induction with increasing radial distance is seen in both measurements and predictions. The “dip” in the measurements within a lateral

interval around zero reflects the presence of the tower for recordings at hub height and below. When measured in terms of rotor plane wind speed, variations of the axial induction over the investigated altitude interval are moderate, reflecting the moderate wind shear. Also observed is a slight left/right asymmetry in the numerical results which, however, is somewhat more pronounced in the measured results. This *systematic* asymmetry is presumable due to a combination of the rotor being tilted 5° and a tangential induction of the sheared inflow. The latter is not included in the numerical predictions, where the asymmetry thus consistently is largest at hub height.

The observed agreement between numerical predictions and measurements confirm the conjecture, that the inherent averaging volume for the LiDAR recordings does not significantly affect the recordings of the rotor plane velocities. This is because the Lorentzian weighting function, associated with the averaging of the LiDAR observations, is approximately symmetric in the vicinity of the rotor plane focus distance, and because the axial induction in the vicinity of the rotor plane, from detailed CFD computations [8] as well as vortex theory based approximations [9], is known to be streamwise anti-symmetric around the rotor location. Therefore, the volume averaging effect, associated with unintentional contributions from recordings symmetrically up- and downstream the intended focus distance, vanish in a first order approximation.

Turning to campaigns 1 and 2 (i.e. Figure 3 and Figure 4), the same general trends are seen as for the campaign 3 results. However, the dependence on altitude is now more pronounced both for measurements and numerical predictions, which might relate to the fact that both changes in the aerodynamic characteristics and in inflow wind speed is in play. Locally large axial induction factors are observed in the measurements, but nowhere the local induction factors exceeds 0.5, which would indicate re-circulation. For the LiDAR recordings referring to normalized altitudes 0.48 and -0.68, respectively, free stream velocities are recorded for large lateral positions, where the measuring volume is outside the rotor plane. Finally, it is noted that the tower is not visible in Figure 4, which is due to the fact that the LiDAR scans in this case refer to altitudes above hub height.

Except for the campaign 2 result, it is further observed, that the rotor plane wind speeds increase with increasing altitude, which is consistent with vertical wind speed profiles shown in Figure 6 conditioned on selected radial positions. Figure 6 moreover display the expected increase in the axial induction with radial distance.

7. Conclusions

We have demonstrated that it is possible to resolve the aerodynamic induction in the rotor plane of an operating wind turbine using a 2D LiDAR technology previously developed for detailed wake studies. The experimentally resolved axial inductions have been compared with analogous numerical predictions based on a BEM approach for three different 10-minute campaigns. The wind turbine operational conditions associated with these campaigns were similar, and the rotor loadings thus of the same order of magnitude. Emphasis was put on selecting runs with moderate fluctuations in the power output, and thus rotor loading, to ensure the best possible accuracy of the induction when based on *mean* inflow and *mean* rotor plane flow characteristics.

The *qualitative* characteristics of measurements and numerical predictions agree well in terms of e.g. increasing induction with increasing radial distance, increasing rotor plane wind speed with increasing altitudes, and *systematic* left/right asymmetry around tower position caused both by rotor tilt and by tangential induction combined with the wind shear. The latter effect is not modelled, and the asymmetry is consequently most pronounced in the measurements. Differences in the *quantitative* agreement are mainly seen in the induction factors, which is a more sensitive measure than the induced velocities in the rotor plane. Locally, large axial induction factors are observed in the measurements, but nowhere the local induction factors exceeds 0.5, which would indicate re-circulation.

8. Acknowledgements
The dataset has been established as a spinoff of wake measurements performed as part of the EU TOPFARM project (Next Generation Design Tool for Optimization of Wind Farm Topology and Operation; Contract REN07/FP6EN/S07.73680/038641). K. Enevoldsen and N. Angelou, Department of Wind Energy, DTU, are acknowledged for assisting in making the analyzed data available.

9. References
[1] Larsen, T.J. and Hansen, A.M. (2007). How to HAWC2, the Users Manual, Risø-R-1597(EN), Risø National Laboratory - Technical University of Denmark.

[2] Bingöl, F.; Mann, J. and Larsen, G.C. (2010). Light detection and ranging measurements on wake dynamics; Part I: One-dimensional Scanning. Wind Energy, **13**, 51-61.

[3] Trujillo, J.J.; Bingöl, F.; Larsen, G.C and Mann, J. (2010). Light detection and ranging measurements on wake dynamics; Part II: Two-dimensional Scanning. Wind Energy, **14**, 61-75.

[4] Gaunaa, M. (2012). Personal communication.

[5] Machefaux, E.; Troldborg, N.; Larsen, G.C.; Mann, J. and Madsen, H.Aa. (2012). Experimental and Numerical study of Wake to Wake Interaction in Wind Farms. EWEC'12, Copenhagen.

[6] Shabana, A. (1998). Dynamics of Multibody Systems, Cambridge University Press.

[7] Madsen, H.Aa.; Riziotis, V.; Zahle, F.; Hansen, M.; Snel, H.; Grasso, L.T.; Politis, E. and Rasmussen, F. (2011). BEM Blade element momentum modeling of inflow with shear in comparison with Advanced Model Results. Wind Energy, **15**(1), 63–81, doi:10.1002/we.493.

[8] Bechmann, A.; Sørensen, N.N. and Zahle. F. (2011). CFD simulations of the MEXICO rotor. Wind Energy, **14**, 677–689, doi:10.1002/we.450.

[9] Medici, D.; Ivanell, S.; Dahlberg, J.-Å. and Alfredsson, P.H. (2011). The upstream flow of a wind turbine: blockage effect. Short Communication. Wind Energy, **14**, 691–697, doi:10.1002/we.451.